Journal of Solid State Chemistry 181 (2008) 2601–2609

Contents lists available at ScienceDirect

Journal of Solid State Chemistry

journal homepage: www.elsevier.com/locate/jssc

Long-range ordering in the $Bi_{1-x}Ae_xFeO_{3-x/2}$ perovskites: $Bi_{1/3}Sr_{2/3}FeO_{2.67}$ and $Bi_{1/2}Ca_{1/2}FeO_{2.75}$

C. Lepoittevin [a,b], S. Malo [a,*], N. Barrier [a], N. Nguyen [a], G. Van Tendeloo [b], M. Hervieu [a]

[a] Laboratoire CRISMAT-ENSICAEN, Bd du Maréchal Juin-14050 CAEN cedex, France
[b] EMAT, University of Antwerp, Groenenborgerlaan 171, B 2020 ANTWERPEN, Belgium

ARTICLE INFO

Article history:
Received 22 February 2008
Received in revised form
23 April 2008
Accepted 28 April 2008
Available online 7 June 2008

Keywords:
Ordered perovskites
Bismuth alkaline earth ferrites
Magneto-transport properties
Mössbauer study

ABSTRACT

Two-ordered perovskites, $Bi_{1/3}Sr_{2/3}FeO_{2.67}$ and $Bi_{1/2}Ca_{1/2}FeO_{2.75}$, have been stabilized and characterized by transmission electron microscopy, Mössbauer spectroscopy and X-ray powder diffraction techniques. They both exhibit orthorhombic superstructures, one with $a \approx b \approx 2a_p$ and $c \approx 3a_p$ (S.G.: *Pb2n* or *Pbmn*) for the Sr-based compound and one with $a \approx b \approx 2a_p$ and $c \approx 8a_p$ (S.G.: *B222*, *Bmm2*, *B2mm* or *Bmmm*) for the Ca-based one. The high-resolution transmission electron microscopy (HRTEM) images evidence the existence of one deficient $[FeO_x]_\infty$ layer, suggesting that $Bi_{1/3}Sr_{2/3}FeO_{2.67}$ and $Bi_{1/2}Ca_{1/2}FeO_{2.75}$ behave differently compared to their *Ln*-based homolog. The HAADF-STEM images allow to propose a model of cation ordering on the *A* sites of the perovskite. The Mössbauer analyses confirm the trivalent state of iron and its complex environment with three types of coordination. Both compounds exhibit a high value of resistivity and the inverse molar susceptibility versus temperature curves evidence a magnetic transition at about 730 K for the $Bi_{1/3}Sr_{2/3}FeO_{2.67}$ and a smooth reversible transition between 590 and 650 K for $Bi_{1/2}Ca_{1/2}FeO_{2.75}$.

1. Introduction

The ABO_3 perovskite structure is known for its ability to accommodate a large variety of structural modifications and for its large variety of chemical and physical properties [1–2]. Among the transition metals occupying the *B* site, iron is the source of a rich chemistry because of its aptitude to adopt different valence states and coordination numbers, able to generate complex structures. The *Ae*–Fe–O systems (Ae = Sr and Ca) are exceptionally rich, evidenced by the existence of the oxygen-deficient perovskites $SrFeO_{3-x}$ [3–8], in which iron atoms adopt the IV, V and VI coordinations. The Fe^{3+}-rich compound ($x = 0.5$), $SrFeO_{2.5}$ [9], exhibits a structure close to $CaFeO_{2.5}$ [3], the aristotype brownmillerite, which is known for its properties of catalytic activity and ionic conduction. The Fe^{4+}-rich compounds ($x = 0$), $SrFeO_3$ and $CaFeO_3$, which exhibit a $GdFeO_3$-type structure at 300 K, are both antiferromagnets [10]. Moreover, the bonding and electronic structure characteristics of the iron-based perovskite doped with trivalent cations give rise to phenomena such as charge and orbital ordering, reported for the $Ln^{3+}_{1/3}Sr_{2/3}FeO_{3-x}$, and multiferroic behavior [11–12]. The magneto-transport properties of different phases resulting from the long and short-range oxygen/vacancies ordering have been extensively investigated; they evidenced a large magneto-resistance and thermoelectric power [13–18].

The bismuth ferrite $BiFe^{3+}O_3$ is also very interesting because of its magneto-electrical properties [19–20] and, contrary to the strontium ferrites, a few studies have been carried out on the substitution of Bi^{3+} by an alkaline earth in this material. In the system Bi–Ba–Fe–O, previous investigations of perovskite derivatives $(Ba_{2-3x}Bi_{3x-1})(Fe_{2x}Bi_{1-2x})O_{2+3/2x}$, have evidenced the existence of very complex oxygen-deficient phases [21–23], in which the trivalent Bi cations are distributed over the two *A* and *B* sites, the cuboctahedral one (with Ba^{2+}) as in $BiFeO_3$ and the octahedral one (with Fe^{3+}) as in $BaBiO_3$ [24–25]. On the other hand, no ordering phenomena have been reported in the Sr and Ca-based systems $Bi_{1-x}Sr_xFeO_3$: one solid solution has been previously reported with a cubic perovskite cell for $Bi_{1-x}Sr_xFeO_3$ with $0.2 \leqslant x \leqslant 0.67$ [26] whereas the rhombohedral symmetry *R3c* is preserved for $Bi_{1-x}Ae_xFeO_3$ (*Ae* = Sr and Ca) perovskites [27] in the range $0 \leqslant x \leqslant 0.2$.

In order to synthesize complex-ordered perovskites in the bismuth alkaline earth-based ferrites, it is important to control as far as possible the two major parameters of stoichiometry. For this purpose, we have investigated the systems $Bi_{1-x}Ae_xFe^{3+}O_{3-x/2}$ (*Ae* = Sr and Ca), keeping the ratio (Bi+*Ae*)/Fe = 1 and a constant value for the valence state of iron (Fe^{3+}). This procedure favors the stabilization of long-range ordering associated to oxygen

* Corresponding author. Fax: +33 231951600.
E-mail address: Sylvie.malo@ensicaen.fr (S. Malo).

0022-4596/$ - see front matter © 2008 Elsevier Inc. All rights reserved.
doi:10.1016/j.jssc.2008.04.047

stoichiometry; the present paper reports the results on $Bi_{1/3}Sr_{2/3}FeO_{2.67}$ and $Bi_{1/2}Ca_{1/2}FeO_{2.75}$.

2. Experimental

The $Bi_{1-x}Ae_xFe^{3+}O_{3-x/2}$ (Ae = Sr and Ca) compositions have been scanned, modifying the synthesis conditions (heating and cooling rate as well as the temperature of the plateau) $Bi_{1/3}Sr_{2/3}FeO_{2.67}$ samples were prepared in a glove box from stoichiometric mixtures of Bi_2O_3, Fe_2O_3, SrO (prepared by the decomposition of $Sr(OH)_2$, $8H_2O$ at 1100 °C and stored at this temperature). $Bi_{1/2}Ca_{1/2}FeO_{2.75}$ samples were prepared from stoichiometric mixtures of Bi_2O_3, Fe_2O_3 and CaO. The precursors were ground in an agate mortar, pressed into bars and sealed in a silica tube. They were heated at 1100 °C for 48 h, with a heating rate of 2 °C/min and slow cooled at the same rate. The as-obtained homogeneous samples were investigated by X-ray powder diffraction and electron diffraction (ED) techniques.

The iron oxidation state was determined by cerimetric titration. The powder X-ray diffraction (PXRD) analyses were carried out at room temperature with a Philips diffractometer using the Cu $K\alpha$ radiation ($\lambda = 1.54180$ Å) in the range $10° \leqslant 2\theta \leqslant 120°$.

The ^{57}Fe transmission Mössbauer spectra for powder samples were measured at room temperature using a ^{57}Co/Rh source.

The ED study was carried out with JEOL 200CX and JEOL 2010 electron microscopes, equipped with eucentric goniometer ($\pm 60°$). The high-resolution transmission electron microscopy (HRTEM) was carried out with a TOPCON 002B microscope, operating at 200 kV (Cs = 0.4 mm), and a JEOL 4000EX microscope, operating at 400 kV. JEOL 200CX, JEOL 2010 and TOPCON 002B microscopes are equipped with energy dispersive spectroscopy (EDS) analyzers. Image calculations were carried out with the Mac Tempas software. High angle annular dark field (HAADF) images were acquired using a JEOL 3000F scanning transmission microscope (STEM)). The high-resolution Z-contrast images make heavier elements appear as brighter dots.

The magnetic measurements were performed by SQUID magnetometry ($T < 400$ K) and the susceptibility measurements with a Faraday balance (0.3 T)· The resistivity was measured using the four-probe method on a Physical Properties Measurements System (PPMS).

3. Results

In the course of the investigation of the $Bi_{1-x}Ae_xFe^{3+}O_{3-x/2}$ systems (Ae = Sr and Ca), two peculiar single-phased compounds have retained our attention, $Sr_{2/3}$ and $Ca_{1/2}$. Their X-ray powder diffraction patterns are given in Fig. 1.

The EDS analyses have been carried out on more than 50 crystallites for each sample. They confirm their homogeneity within the accuracy limit of the technique. The actual cationic Bi/*Ae*/Fe ratios are 1/2/3 for the Sr-based compound and 1/1/2 for the calcium-based one. For the two ferrites, the cerimetric titration led to a trivalent oxidation state of iron, in the limit of accuracy of the technique. The total composition of the two title compounds is $Bi_{1/3}Sr_{2/3}FeO_{2.67}$ and $Bi_{1/2}Ca_{1/2}FeO_{2.75}$ (the standard deviations are $Bi_{0.33(6)}Sr_{0.67(6)}$ and $Bi_{0.5(3)}Ca_{0.5(3)}$ calculated for one iron atom per unit).

3.1. Determination of the supercell

3.1.1. $Bi_{1/3}Sr_{2/3}FeO_{2.67}$

The ED patterns of all the crystallites exhibit a first set of intense reflections, corresponding to a perovskite subcell (with $a_p \approx 3.95$ Å, the suffix "p" refers to the perovskite unit cell). Besides

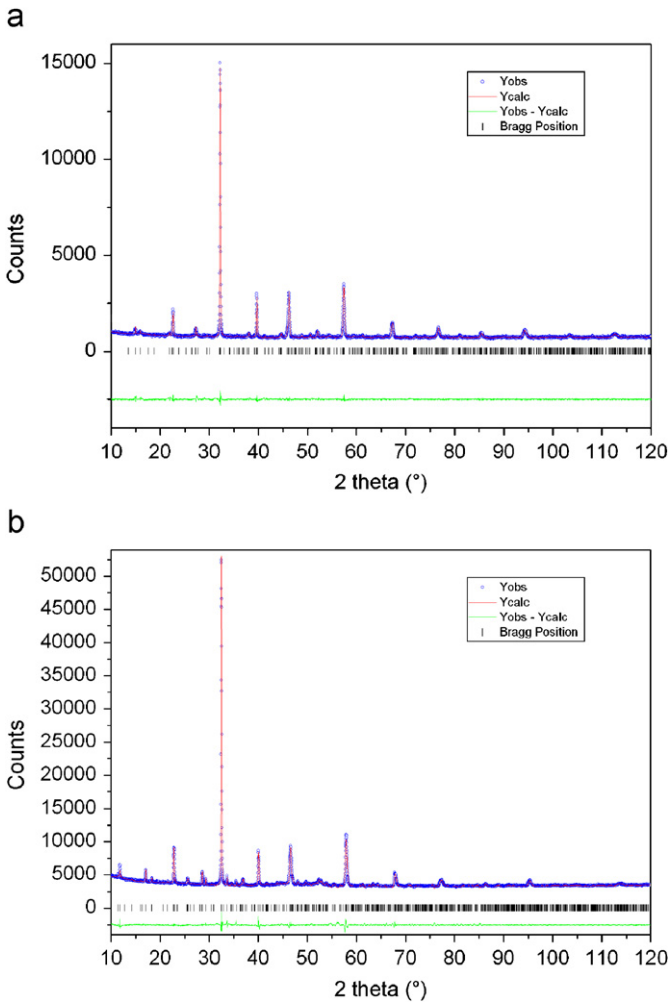

Fig. 1. X-ray powder diffraction patterns of (a) $Bi_{1/3}Sr_{2/3}FeO_{2.67}$ and (b) $Bi_{1/2}Ca_{1/2}FeO_{2.75}$.

these fundamental reflections, a second system of extra reflections is observed, characteristic of a commensurate orthorhombic superstructure with $a \approx b \approx 2a_p$ and $c \approx 3a_p$. A typical ED pattern (Fig. 2a) illustrates the micro-structural state of the material. It is characteristic of twinning and of the coexistence of the different variants, resulting from the geometrical relationships between the parameters (pseudo-cubic perovskite subcell) and the lowering of the symmetry. The HRTEM images of the crystallites (Fig. 2b) show that the size of the oriented domains commonly ranges between a few tens to a few hundred nanometers. A determination of the forbidden reflections was therefore rather difficult to perform due to an overlap of the tinny twin domains. The reconstruction of the reciprocal space was carried out by tilting around the major crystallographic axes, selecting as far as possible non-overlapping variants. Our analysis was completed through fast Fourier transforms (FFT) on selected zones of the HREM images. The latter results are illustrated in Fig. 3, which present the [010], [100] and [001]-oriented zones. The conditions limiting the reflection are hkl: *no cond*, $h0l$: *no cond* (Fig. 3a), $hk0$: $h+k = 2n$ (Fig. 3b) and $0kl$: $k = 2n$ (Fig. 3c), leading to an orthorhombic supercell ($2a_p \times 2a_p \times 3a_p$) and *Pb*2*n* or *Pbmn* as possible space groups. The superposition of the six possible variants perfectly explains the complexity of the ED pattern generally observed for this material (Fig. 2a). The cell parameters have been refined considering the space group *Pbmn*, using the program JANA2006 [28]; they are given in Table 1.

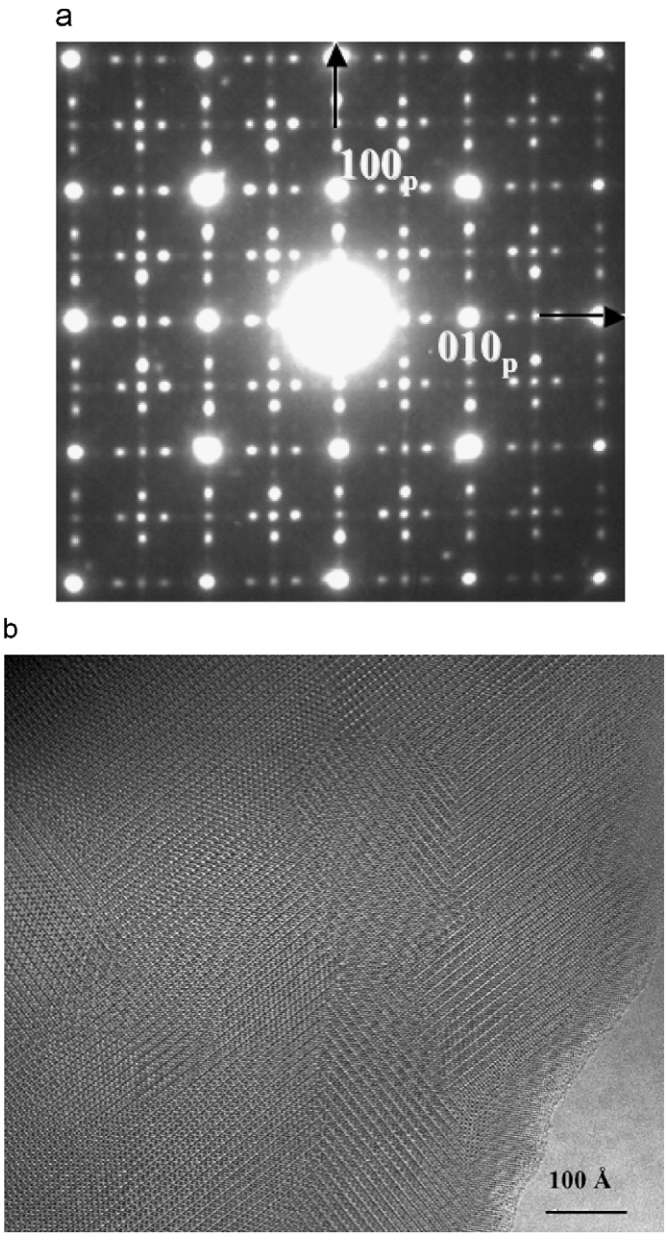

Fig. 2. $Bi_{1/3}Sr_{2/3}FeO_{2.67}$: (a) typical ED pattern resulting from the overlapping of different variants and (b) corresponding HRTEM image illustrating the size and arrangement of the twin domains.

3.1.2. $Bi_{1/2}Ca_{1/2}FeO_{2.75}$

Similar to the strontium-based ferrite, the reconstruction of the reciprocal space evidenced a first set of intense dots corresponding to a perovskite subcell (with $a_p \approx 3.9$ Å) and a second system of extra reflections characteristic of a commensurate orthorhombic superstructure with $a \approx b \approx 2a_p$ and $c \approx 8a_p$. The only condition limiting the reflection, $h\,k\,l$: $h+l = 2n$, involves *B*222, *Bmm*2, *B*2*mm*, *Bmmm* as possible space groups; the [100], [010], [001] and $[1\bar{1}0]$ ED patterns are given in Fig. 4. The cell parameters, refined considering the space group *Bmmm*, are given in Table 1.

In both ordered phases, the periodicity along $\vec{c}$ is directly related to the oxygen stoichiometry, consequence of the ratio between the trivalent and the divalent cations occupying the *A* site. Such an effect is commonly observed in Fe^{3+}-based perovskites, such as for example $Sr_2LaFe_3O_8$ [29] and in several other brownmillerite-related oxides, which can be directly compared to the title compound $Bi_{1/3}Sr_{2/3}FeO_{2.67}$. However, the $Ln_{1/3}Ae_{2/3}FeO_{2.67}$ ferrites, i.e. $LnAe_2Fe_3O_8$, generally adopt an oxygen atoms/vacancies ordering-mode along the $[110]_p$ direction of the perovskite subcell, associated to a tetrahedral environment of the iron atoms in the deficient layer (labeled "T"), sandwiched between two octahedral layers (labeled "O"); this structure corresponds to the configuration T–O–O– ($a_p\sqrt{2} \times a_p\sqrt{2} \times 3a_p$). In the bismuth-based compounds, $Bi_{1/3}Sr_{2/3}FeO_{2.67}$ and $Bi_{1/2}Ca_{1/2}FeO_{2.75}$, the ordering directions perpendicular to $\vec{c}$ are different ($2a_p \times 2a_p$), suggesting that the formation of tetrahedral layers is not the main driving mechanism. This is also the case of the Ba-based ordered structure $Bi_{1/2}Ba_{1/2}FeO_{2.75}$, for which a tetragonal supercell $a_p \times a_p \times 4a_p$ is found. The different a_p parameters of the subcell of each of the three-ordered $Bi_{1-x}Ae_xFe^{3+}O_{3-x/2}$ perovskites are summarized in Table 2. One observes a regular increase of the subcell volume, in agreement with the average radius of the *Ae* cations.

3.2. ^{57}Fe Mössbauer study

In order to confirm the valence state of the iron ions and to investigate their environment, ^{57}Fe transmission Mössbauer spectra for $Bi_{1/3}Sr_{2/3}FeO_{2.67}$ and $Bi_{1/2}Ca_{1/2}FeO_{2.75}$ powder samples were measured at room temperature using a ^{57}Co/Rh source. The isomer shifts (IS) are corrected for the room temperature IS of metallic iron taken as a reference. The magnetic spectra have been simulated using a least-square fitting routine assuming a Lorentzian line shape called MOSFIT [30].

For $Bi_{1/3}Sr_{2/3}FeO_{2.67}$, the better fit of the spectrum (Fig. 5) requested three Mössbauer sextuplets noted *A*, *B* and *C*. Their

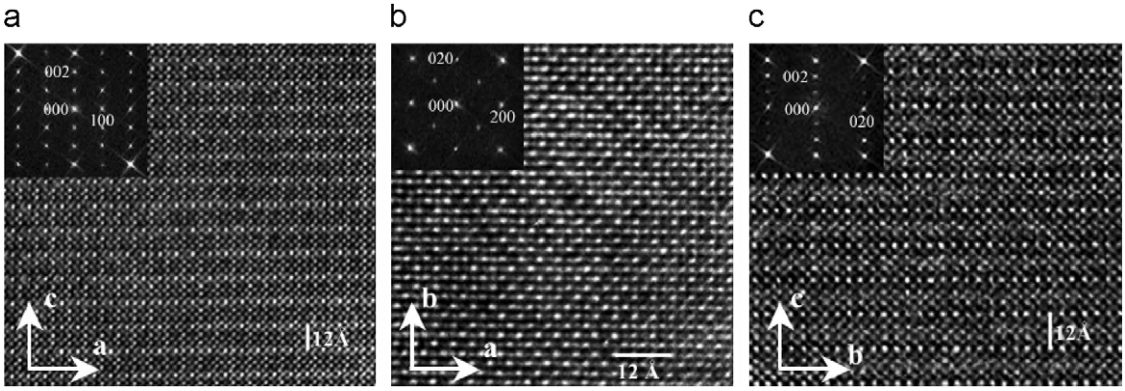

Fig. 3. $Bi_{1/3}Sr_{2/3}FeO_{2.67}$: HREM images and fast Fourier transforms (FFT) of non-overlapped domains (a) [010], (b) [001] and (c) [100].

Table 1
Refined parameters of the ordered perovskite cells

Compound	a (Å)	b (Å)	c (Å)	S.G.
$Bi_{1/3}Sr_{2/3}FeO_{2.67}$	7.890(10)	7.852(6)	11.871(7)	*Pb2n*, *Pbmn*
$Bi_{1/2}Ca_{1/2}FeO_{2.75}$	7.8284(2)	7.8112(3)	31.1490(8)	*B222*, *Bmm2*, *B2mm*, *Bmmm*

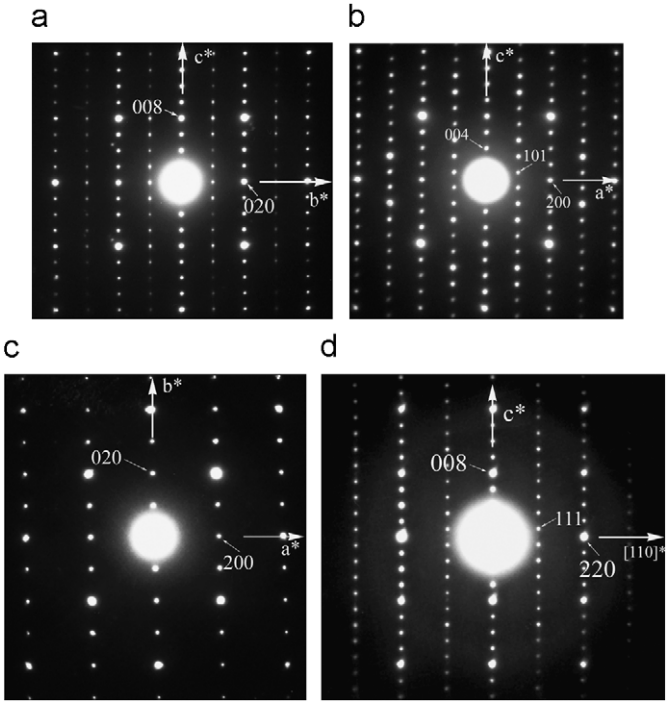

Fig. 4. $Bi_{1/2}Ca_{1/2}FeO_{2.75}$: ED patterns corresponding to (a) [100], (b) [010], (c) [001] and (d) [1 $\bar{1}$ 0].

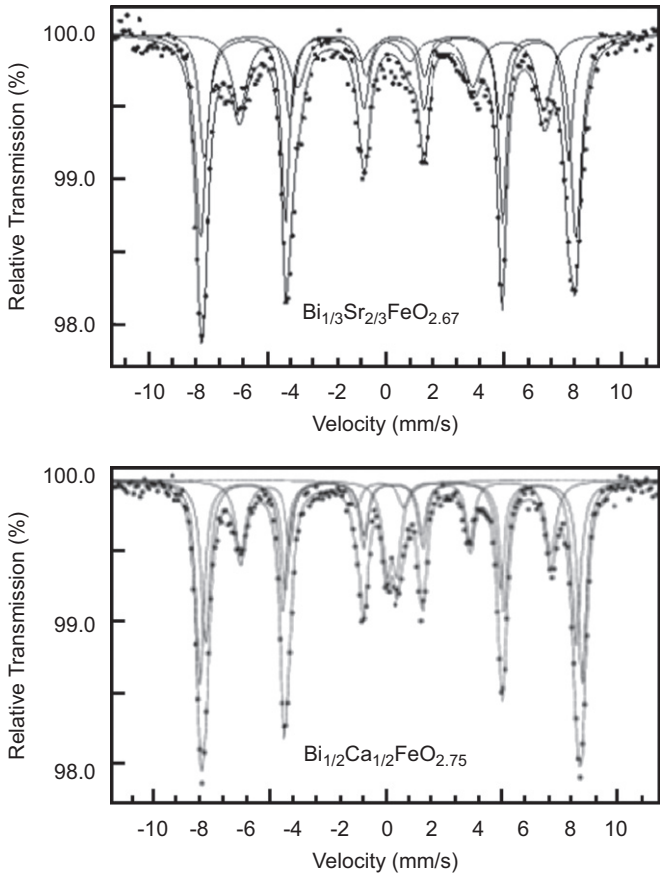

Fig. 5. ^{57}Fe transmission Mössbauer spectra for $Bi_{1/3}Sr_{2/3}FeO_{2.67}$ and $Bi_{1/2}Ca_{1/2}FeO_{2.75}$.

Table 2
Compared perovskite subcells of the three-ordered $Bi_{1-x}Ae_xFe^{3+}O_{3-x/2}$ perovskites

Compound	$(a_p \times a_p) \times a_p$	V (Å^3)	Average r_A^{XII} (Å)[a]	Ref.
$Bi_{1/2}Ba_{1/2}FeO_{2.75}$	$(3.98 \times 3.98) \times 4.09$ Å^3	64.79	1.49	[22–23]
$Bi_{1/3}Sr_{2/3}FeO_{2.67}$	$(3.95 \times 3.92) \times 3.96$ Å^3	61.32	1.41	This work
$Bi_{1/2}Ca_{1/2}FeO_{2.75}$	$(3.92 \times 3.91) \times 3.89$ Å^3	59.62	1.35	This work

[a] On the basis of a r_{Bi}^{XII} value $\approx$ 1.36 Å and RD Shannon 1976.

hyperfine parameters are given in Table 3. One observes that the *A* and *B* components have similar fitted IS values (about 0.35 mm/s), and the same negative sign of the quadrupole shifts ($2\varepsilon = -0.21$ and -0.35 mm/s, respectively). The IS and the hyperfine field ($H_f = 49.3$ and 47.7 T) values of both sites are typical of high spin trivalent iron ions. However, the gap between H_{fA} and H_{fB} and between the 2ε values of both sites are quite significant, suggesting that their symmetries are different. So, it is reasonable to attribute the *A* site, with the highest H_f and the lowest $|2\varepsilon|$ values, to an octahedral environment, and the *B* site to a pyramidal coordination.

While for the *C* component, the lower IS and H_f values (IS = 0.23 mm/s, $H_f = 39.9$ T) indicate that it corresponds to a more Fe^{3+} distorted environment, its symmetry is noticeably reduced compared to the *A* and *B* components. This is related to the existence of the variable nucleus-ligands angles ($\langle$O–Fe–O$\rangle$) and distances (Fe–O) in the *C* coordination polyhedron. This symmetry reduction suggests that *C* could correspond either to an iron tetrahedral environment or a pyramidal one which is more distorted than B. Anyway, due to the very weak satellite peaks in the diffraction pattern, the structural calculations did not allow us to evidence the existence of a tetrahedral coordination. Therefore, *C* could correspond to a distorted pyramidal site.

The relative intensities of *A*, *B* and *C* contributions obtained by the Mössbauer spectrum simulation show that 49% of Fe^{3+} are in an octahedral environment and 51% (29% for *B*; 22% for *C*) in pyramidal sites.

In the case of $Bi_{1/2}Ca_{1/2}FeO_{2.75}$, it is necessary to introduce four Mössbauer components (noted *A*, *B*, *C* and *D*) (Fig. 5) to obtain an accurate result for the fit of its spectrum. The three *A*, *B* and *C* sites are magnetic, their IS and H_f values (Table 3) are in the same value ranges as for the Sr compound. These hyperfine parameters of *A* (IS = 0.38 mm/s; $H_f = 50.9$ T) are characteristic of high spin Fe^{3+}. Its small 2ε value (-0.09 mm/s) shows that this site corresponds to a symmetrical octahedral environment. With respect to the *A* parameters, the IS and H_f values of *B* contribution are slightly reduced (0.36 mm/s and 49.4 T, respectively) leading to a symmetry lowering of the Fe nucleus. Consequently, the *B* environment could be a regular pyramid. Compared to the *A* and

Table 3
RT fitted hyperfine Mössbauer parameters of $Bi_{1/3}Sr_{2/3}FeO_{2.67}$ and $Bi_{1/2}Ca_{1/2}FeO_{2.75}$

IS ± 0.01 (mm/s)	$2\varepsilon \pm 0.01$ (mm/s)	$H_f \pm 0.1$ (T)	Site relative intensity % ± 3	Fe^{3+} environment
$Bi_{1/3}Sr_{2/3}FeO_{2.67}$				
0.36	−0.21	49.3	49	A—Octahedral
0.35	−0.35	47.7	29	B—Pyramidal
0.23	0.29	39.9	22	C—Distorted pyramidal
$Bi_{1/2}Ca_{1/2}FeO_{2.75}$				
0.37	0.47[a]		9	D—Paramagnetic
0.38	−0.09[a]	50.9	41	A—Octahedral
0.36	−0.07[a]	49.4	30	B—Pyramidal
0.19	0.69[a]	41.5	20	C—Distorted pyramidal

[a] Quadrupolar splitting QS in the paramagnetic state.

B results, the *C* component accepts a smaller IS value (0.19 mm/s) and a clearly higher 2ε one (0.69 mm/s), which suggests to think that the environment of this site is much more distorted.

This result is also in agreement with the strongly decrease of its H_f value (41.5 T). Therefore, we can attribute a distorted pyramidal coordination to *C* site. The relative intensities of the three main *A*, *B* and *C* contributions are 41%, 30% and 20%, respectively.

At last, the fourth Mössbauer component (*D*) is paramagnetic. Its small intensity ($\approx$9%) leads to think that this additional component could be from an iron-containing impurity phase but maybe in the amorphous state.

3.3. Electron microscopy study

(i) High-resolution transmission electron microscopy

The contrast of HRTEM images is very sensitive to structural modifications such as cation ordering, oxygen vacancies and atomic displacements. Therefore, a direct correlation of a focus series with a given ordered structure is not straightforward. In a first step, we focused on two typical contrasts commonly observed in ordered oxygen-deficient perovskites; they are displayed in Fig. 6a and b, and have been recorded along [100] for two characteristic focus values.

The experimental images of $Bi_{1/2}Ca_{1/2}FeO_{2.75}$ have been compared to the simulated images calculated for an hypothetical structure based on the structure of $Bi_{1/2}Ba_{1/2}FeO_{2.75}$; the Ba^{2+} cations have been replaced by Ca^{2+} [23] and the supercell parameters $a_p \times a_p \times 4a_p$ (SG: *P*4/*mmm*) calculated using the Ca-based unit cell (Table 2). The reason for this choice is based on the similarity of the oxygen stoichiometry, the presence of the Bi^{3+} in the *A* site and the tetragonal $a_p \times a_p$ arrangement. In this first step, this allows freeing from a tetrahedral-deficient oxygen layer.

In Fig. 6a, the bright dots are associated to the cation positions (focus value close to −47 nm) and the darker rows (spaced by 15.6 Å $\approx c/2$ along $\vec{c}$) are associated to the existence of an oxygen-deficient $[FeO_x]_\infty$ layer ($x \approx 1.5$ in [23]). In Fig. 6b, the high electron density zones appear as the darker dots and the oxygen-deficient $[FeO_x]_\infty$ layer as a row of brighter dots (focus values close to −15 nm). A similar contrast is also observed for $Bi_{1/3}Sr_{2/3}FeO_{2.67}$, the brighter rows associated to the oxygen-deficient $[FeO_x]_\infty$ layers being spaced by $3a_p$ along $\vec{c}$ (Fig. 3c). Viewing $Bi_{1/2}Ca_{1/2}FeO_{2.75}$ along [010] (Fig. 6c) for a focus value close to Scherzer focus, the cation positions appear as dark dots, the rows of Bi and Ca cations are indicated by white arrows; they sandwich three rows of iron exhibiting an even contrast. Every 15.6 Å ($c/2$) along $\vec{c}$, one row of iron cations

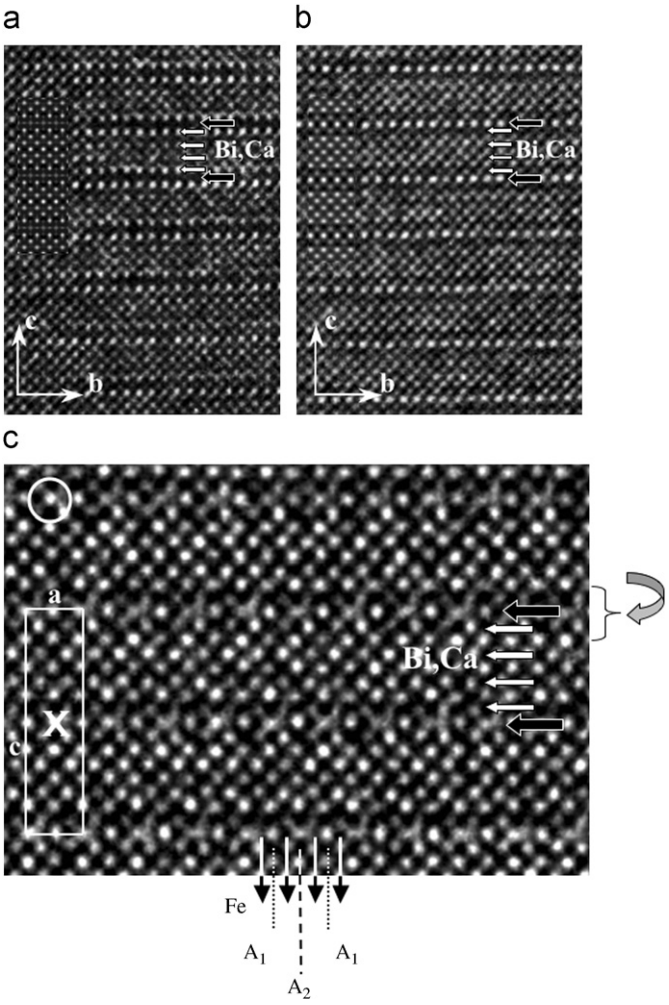

Fig. 6. $Bi_{1/2}Ca_{1/2}FeO_{2.75}$: [100] HREM image (a) the bright dots are associated to the cation positions and the darker rows to the $[FeO_x]_\infty$ layer. (b) The oxygen-deficient $[FeO_x]_\infty$ layer appears as the row of brighter dots. (c) [010] HRTEM image: the Bi/Ca layers are indicated by white arrows and the $[FeO_x]_\infty$ layer by a black one. One bright spot alternates with a blurred one forming an X sign in the layer. The positions of the cations of this layer and those of the two adjacent ones (A_1 and A_2) are indicated.

(see the black arrow) exhibits a peculiar contrast; it consists in the alternation of one bright spot with a blurred one forming a X sign (schematized in Fig. 6c) with the four adjacent ones belonging to the upper and lower rows. These variations of

contrast at the level of the iron polyhedra, as well as the variations between the iron positions that they involved (see the vertical arrows in the enlarged Fig. 6c), can be associated with an oxygen atoms/vacancies ordering along the [100] direction of the structure. The [010] images show that these contrast variations and atomic displacements are also propagating into the two adjacent [(Bi,Ca)O] layers, suggesting that an ordering phenomenon could take place; the ordered cation sites are denoted as A_1 and A_2 in Fig. 6c.

A first and very simple model is presented in Fig. 7a; it only aims to propose the existence of one peculiar block (denoted "Or/D"), likely made of more or less anion and cation-ordered layers (one $[FeO_x]_\infty$ sandwiched between two $[(Bi,Ca)O]_\infty$), which alternates along $\vec{c}$ with one regular perovskite slice (denoted "R").

Note that the *B* centering is locally violated by point-like defects as indicated by the circle in Fig. 6c.

(ii) HAADF-STEM imaging

One efficient way to study atomic-ordering phenomena is to record HAADF-STEM images, for which the brightness increases, approximately proportional to Z^2 [31]. In the as-obtained images, the heavy atoms are imaged as bright dots and the contribution of light atoms is negligible. In our compounds, the presence of bismuth is a favorable parameter to obtain information on the contrast generated by the cation ordering, ignoring the contribution of the oxygen lattice.

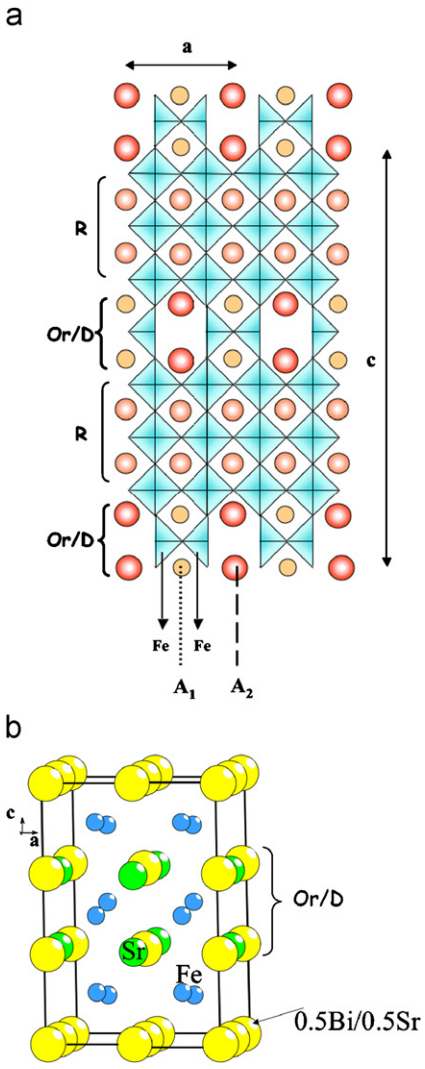

Fig. 7. (a) $Bi_{1/2}Ca_{1/2}FeO_{2.75}$: hypothetical simple model deduced from the TEM images. It proposes the existence of one peculiar block made of likely anion and cation-ordered $[FeO_x]_\infty$ sandwiched between two $[(Bi,Ca)O]_\infty$ layers. (b) Model proposed for the stacking of the cation layers in $Bi_{1/3}Sr_{2/3}FeO_{2.67}$ from the XRPD. Two layers are composed of one site (1Sr) and one mixed site and one layer has only one mixed site (0.5Bi/0.5Sr).

3.3.1. $Bi_{1/3}Sr_{2/3}FeO_{2.67}$

[001]-oriented HAADF-STEM image is shown in Fig. 8a. On the lower right hand corner, a contrast consisting of an alternation of very bright and weaker dots is observed along the [100] and [010] directions. The bright dots can be associated to the projection of Bi–Sr columns with a high Bi contribution, whereas the weaker dots correspond to Bi–Sr columns with a high Sr contribution. Such an alternation of bright and weak dots along the [100] and [010] direction suggests that Bi and Sr are ordered on the (001) main zone, leading to a doubling of the perovskite parameters. The FFT of this part of the image exhibits a centering, resulting in a doubling of the *a* and *b* parameters caused by the Bi–Sr ordering on the *A* sites.

However, such a significant difference of contrast is not so clearly observed in other parts of the image where the brightness of the dots appears equal. The corresponding FFT (upper inset) shows no centering, with a local $a_p \times a_p$ periodicity in the basal plane, similar to the Ba-based ferrite. Note that such local variations are hard to detect by ED due to the overlap of the twin domains (Fig. 2a). These observations evidence that the Bi–Sr ordering is locally destroyed.

3.3.2. $Bi_{1/2}Ca_{1/2}FeO_{2.75}$

The [010] HAADF-STEM image in Fig. 8b exhibits a contrast close to the HRTEM image showing the high electron density as bright dots (Fig. 6a). Every 15.6 Å ($\approx c/2$), two rows consisting of an alternation of bright dots with weaker dots along the [100] direction appear, surrounding a darker row associated to the oxygen-deficient layer $[FeO_x]$ (pointed out by black arrows in Fig. 8b). The weaker dots are related to the projections of Bi–Ca ordering along the [010] direction, responsible of the doubling of the *b* parameter and the brighter dots can be associated to the Bi columns. Such an ordering between Bi–Ca and Bi columns along the [100] direction can explain the doubling of the *a* parameter as well as the displacement of the oxygen atoms forming an X visible on the HTREM image presented in Fig. 6c. These HAADF images complement the HTREM observations, confirming the ordering between Bi-rich and Sr-rich sites in two adjacent [AO] layers sandwiching one peculiar iron layer and the existence of a random distribution of the two cations in the other sites of the structure.

3.4. X-ray powder diffraction study

Different attempts have been made to determine a structural model by a direct method.

3.4.1. $Bi_{1/3}Sr_{2/3}FeO_{2.67}$

Whole X-ray powder pattern refinements with cell constraint were performed in an orthorhombic unit cell with *Pb2n* and *Pbmn* space groups. Fig. 1a presents the results of the pattern refinement in the *Pbmn* space group (gof = 1.13; $R_p = 2.99$; $R_{wp} = 3.95$). Inspection of the profile reveals a stronger broadening for reflections of the superstructure. Extraction of the structure factor moduli using the Le Bail method was carried out with the Jana2006 program [28] and direct method procedures were then performed with the Expo program [31] for these two space groups. The best solution was found for the *Pbmn* space group

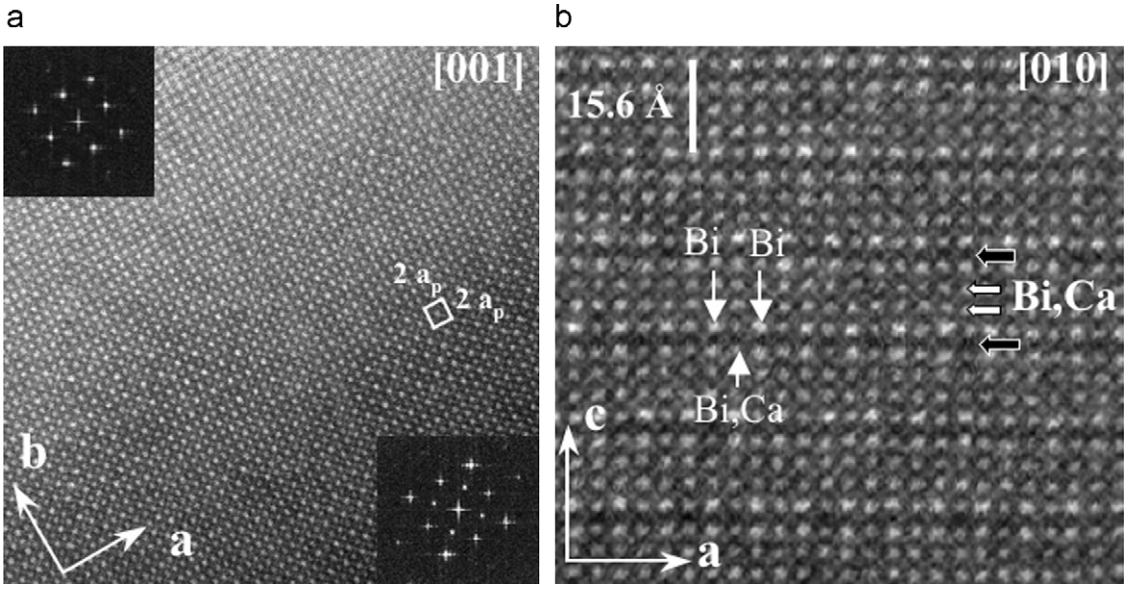

Fig. 8. HAADF-STEM images: (a) for $Bi_{1/3}Sr_{2/3}FeO_{2.67}$, the alternation of bright and weak dots suggests that Bi and Sr are mainly ordered along the [100] and [010] direction (lower zone), but the image also evidences defective areas (upper zone) and (b) for $Bi_{1/2}Ca_{1/2}FeO_{2.75}$, along [100], an ordering between Bi–Ca and Bi columns explains the doubling of the *a* parameter.

with a reliability factor $R_F = 13.01\%$ and all the crystallographic positions of heavy atoms Bi/Sr and Fe have been determined. This first model confirms the perovskite-related structure of $Bi_{1/3}Sr_{2/3}FeO_{2.67}$. For the first Rietveld refinements, mixed Bi/Sr sites were considered since the previous solution did not show any order between the Bi and Sr atoms. The oxygen positions were introduced in respect of the octahedral environment of the Fe atoms of the perovskite-type structure. After several refinements of crystallographic positions and the ratio Bi/Sr for all mixed sites we have obtained a model with a structure factor $R_{obs} = 6.57\%$ and profile factors $R_{wp} = 4.39\%$; gof = 1.26. At this time it appears that one crystallographic site could be fully occupied by strontium atoms but the refinements of the oxygen positions are very unstable. Thus a first stacking of the cation layers can be proposed as presented in Fig. 7b. Two layers composed by one site (1Sr), fully occupied by strontium, and one mixed site (0.5Bi/0.5Sr) alternate with one layer of only mixed sites (0.5Bi/0.5Sr). The theoretical images (not presented here) calculated with the positions of this first model fit with the experimental images where the cation positions are highlighted. Nevertheless this model should be considered with precaution since the oxygen positions are uncertain. Neutron powder diffraction studies have to be performed to find the precise oxygen positions and completely resolve this structure.

3.4.2. $Bi_{1/2}Ca_{1/2}FeO_{2.75}$

For this compound, whole pattern refinements with cell constraint and Le Bail decomposition were performed in an orthorhombic unit cell with *B*222, *Bmm*2, *B*2*mm* and *Bmmm* space groups with the Jana2006 program. Fig. 1b presents the results of the pattern refinement in the *Bmm*2 space group (gof = 1.24; $R_p = 1.45$; $R_{wp} = 2.03$).

The refinement of the crystal structure is very difficult because of the large cell parameters that imply, a huge number of independent crystallographic parameters, on the one hand, and the overlapping of a lot of diffraction peaks, on the other hand. A second difficulty is due to the small size of twin domains, which produces a broadening of the reflections. Nevertheless, Rietveld refinements were carried out starting from the previous model $Bi_{1/2}Ca_{1/2}FeO_{2.75}$ constructed from the TEM study (Fig. 7a). In a first time, the A_1 and A_2 sites were considered fully occupied by Ca and Bi atoms, respectively, with a mixed occupancy 50%Bi and 50% Ca in the sites of the *R* slice. Refinements of the Bi, Ca positions assuming, the same U_{iso} parameters for all Bi and Ca positions and same U_{iso} for the four Fe atoms yield to poor *R* factors. The improvement of the refinements was obtained by assuming mixed occupancy Bi/Ca for all the bismuth and calcium sites. The refinement of the occupancy parameters yield to relative good *R* factors ($R_{obs} = 7.01\%$ $R_{wp} = 2.56$; gof = 1.57) and it appears in agreement with the TEM observation, that the A_1 site are mainly occupied by Ca atoms (67.5% Ca and 32.5% Bi) and the A_2 sites are mainly occupied by the Bi atoms (66.5% Bi and 33.5% Ca). The average occupancy of the *R* slice sites is 50%Bi/50%Ca. Finally, the accurate localization of the oxygen atoms appears extremely difficult due to the fact that X-ray powder diffraction is not very sensitive to the presence of oxygen vacancies and to the order–disorder phenomena detected by TEM techniques. Thus we have just maintain tetrahedral environment for Fe atoms in the Or/D layer and octahedral environment for the other ones.

Despite the fact that small single crystals have been grown, we have not succeeded to refine the ordered structure; this mainly because of the tiny sizes of the twin domains.

3.5. Magnetic and transport properties

The evolution of the inverse molar susceptibility versus temperature during heating is given in Fig. 9a for $Bi_{1/3}Sr_{2/3}FeO_{2.67}$. It evidences a magnetic transition at about 730 K. In our experimental conditions limited to 800 K, the linear paramagnetic regime is not reached. In Fig. 9b, the inverse molar susceptibility versus temperature is given for the ferrite $Bi_{1/2}Ca_{1/2}FeO_{2.75}$ during heating and cooling; the reversible transition is smooth and is observed between 590 and 650 K. These results can be compared to those obtained for $Bi_{1/2}Ba_{1/2}FeO_{2.75}$, which showed a transition from a magnetic state towards a paramagnetic state in a large domain of temperature ranging between 620 and 720 K. The

nuclear structure refinement, carried out from neutron diffraction data, allowed to determine [23] an AFM state, the magnetic moment being aligned in the (*ab*) plane.

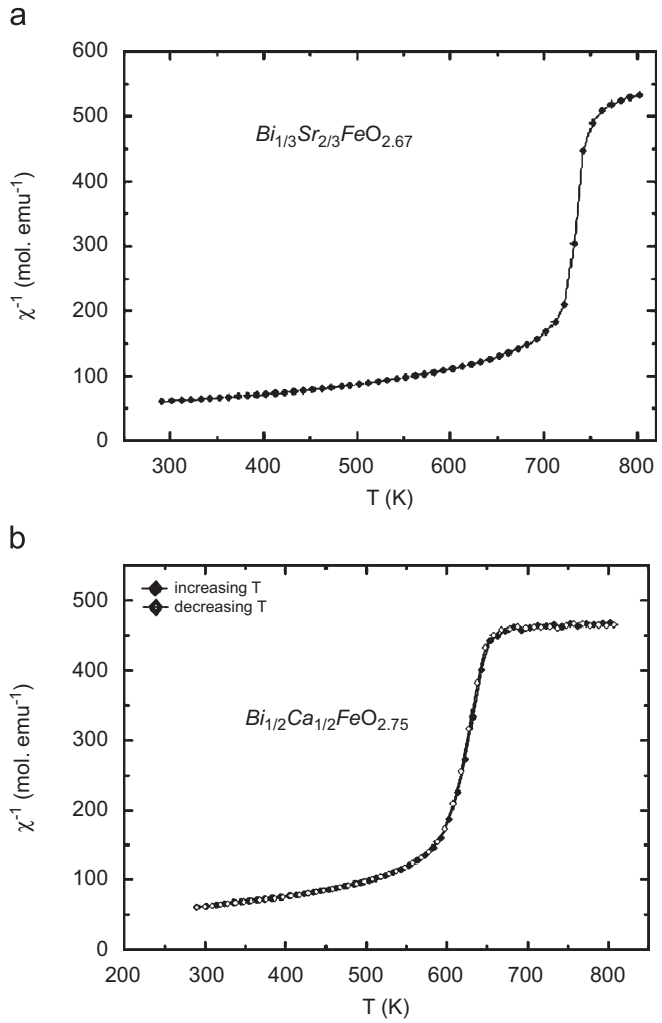

Fig. 9. Inverse molar susceptibility versus temperature for (a) $Bi_{1/3}Sr_{2/3}FeO_{2.67}$ (the paramagnetic regime is not reached) and (b) $Bi_{1/2}Ca_{1/2}FeO_{2.75}$.

Contrary to the solid-solution $Sr_{1-x}Bi_xFeO_3$, which is characterized by a mixed valence of iron, such a behavior can be compared to that of the ortho-ferrites $LnFe^{3+}O_3$, which are characterized by an AFM state due to a strong coupling Fe^{3+}–O–Fe^{3+} at 180° and high Néel temperature of 750, 760, 700 and 620 K for La [32], Nd, Ho and Er, respectively [33]. The AFM configurations of the spins in these compounds have been reported of the G-type, as well as the one of the $BiFeO_3$ ferrite [20], with $T_N = 643$ K and a ferroelectric order at $T_c = 1103$ K. The rhombohedrally distorted $Bi_{0.7}Ae_{0.3}FeO_3$ (Ae = Sr and Ca) perovskites [27–36] have been reported to reproduce an antiferromagnetic behavior similar to the undoped parent material.

The rare-earth strontium-based ferrites $Ln_{1/3}Sr_{2/3}FeO_{3-\delta}$ (Ln = La [34], Pr [35] Sm [9], which crystallize in distorted perovskite-type structures, exhibit significantly lower T_N, 207 K for La and 150 K for Sm for small δ value. They have the particularity to present charge ordering at low temperature ($2Fe^{4+} \Leftrightarrow Fe^{3+}+Fe^{5+}$) but T_N increases up to 700 K as δ increases (as the amount of Fe^{3+} increases).

The resistivity and the activation energy as a function of the temperature for $Bi_{1/2}Ca_{1/2}FeO_{2.75}$ are given in Fig. 10a and b, respectively. The high value of resistivity involves a semiconducting or insulating behavior; similar results are obtained for the compound $Bi_{1/3}Sr_{2/3}FeO_{2.67}$. In the same way, the high value of activation energy (about 0.32 eV) is in agreement with an antiferromagnetic-type state.

3.6. Discussion and concluding remarks

Two-ordered perovskites $Bi_{1/3}Sr_{2/3}FeO_{2.67}$ and $Bi_{1/2}Ca_{1/2}FeO_{2.75}$ have been stabilized by controlling the oxygen stoichiometry, with 12-fold ($a \approx b \approx 2a_p$ and $c \approx 3a_p$) and 32-fold ($a \approx b \approx 2a_p$ and $c \approx 8a_p$) enlargements of the perovskite unit cell, respectively. In both compounds, the Mössbauer spectra evidence a complex coordination of the trivalent iron atoms with at least three types of environment, namely octahedral, pyramidal and tetrahedral. The complex ordering phenomena have been studied using different electron microscopy techniques, which provide important information.

The HRTEM images suggest the existence of deficient $[FeO_x]_\infty$ layers: one out of three for $Bi_{1/3}Sr_{2/3}FeO_{2.67}$ and one out four for $Bi_{1/2}Ca_{1/2}FeO_{2.75}$. However, the iron polyhedra arrangements

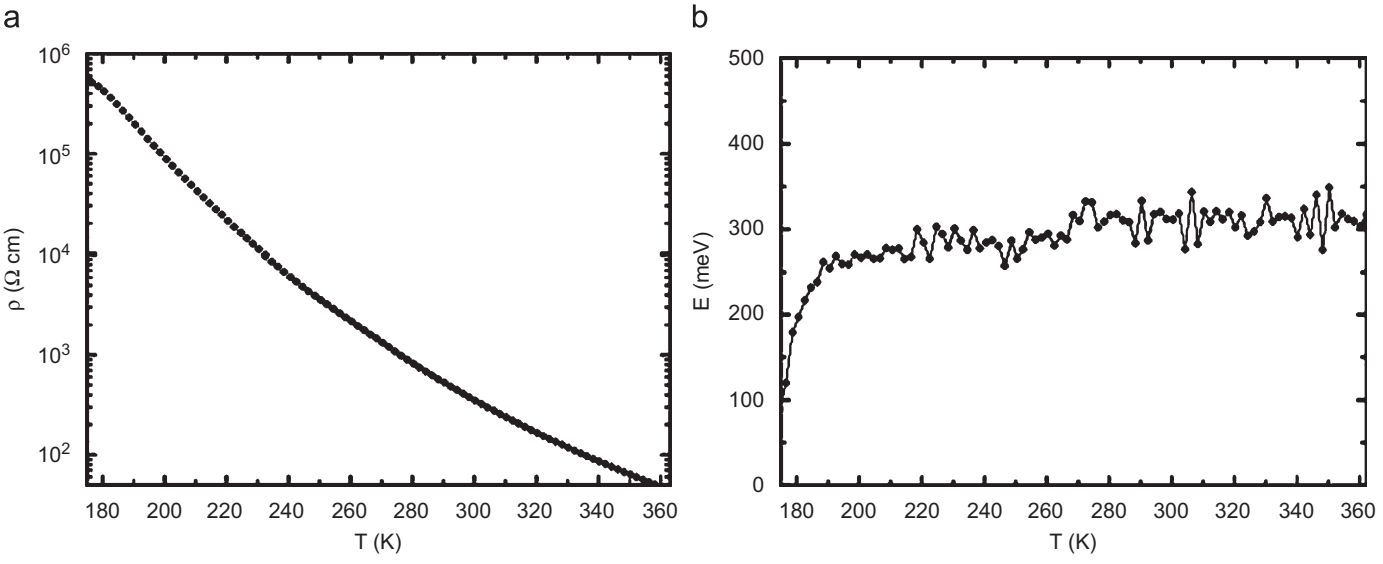

Fig. 10. (a) Resistivity and (b) activation energy as a function of the temperature for $Bi_{1/2}Ca_{1/2}FeO_{2.75}$.

would be different from those commonly observed for the isocompositional $Ln_{1-x}Ae_xFe^{3+}O_{3-x/2}$ ferrites ($x = 1/3$ and $1/2$), built up from the simple alternation of tetrahedral (“T”) and octahedral (“O”) layers. They also suggest the existence of two types of alternating blocks (or slices) denoted “Or/D” and “R”. The first ones are characterized by more or less ordered anions and cations, and are likely made of one oxygen-deficient $[FeO_x]_\infty$ layer sandwiched between two-ordered $[(Bi/Ca)O]_\infty$ layers. The second one corresponds to a perovskite slice, exhibiting a regular contrast suggesting that cations and oxygen/vacancies (which should exist if one considers the formulation and the Mössbauer results) are randomly distributed on their own sites. These observations have been confirmed by the HAADF-STEM images, which evidenced the Bi/Ca ordering in the two layers sandwiching the $[FeO_x]_\infty$ layer, whereas the uniform contrast at the level of the other $[(Bi,Ca)O]_\infty$ layers is in agreement with a random distribution of the two cations. In the case of $Bi_{1/3}Sr_{2/3}FeO_{2.67}$, the HRTEM study and the first XRPD model are in agreement with the hypothesis of an alternation of “Or/D” and “R” slices. In the later case, the “R” would consist of a single perovskite layer whereas the ordering in the “Or/D” slice corresponds to the alternation along [100] and [010] of “Bi-rich” and “Sr-rich” occupied sites. However, the HAADF-STEM images showed that the calculated occupancy factors can be biased by the existence of local disappearance of the Bi/Sr ordering.

The existence of cation ordering in the *A* sites of the Bi-based perovskites is of interest. It is known that the cations and vacancies ordering is frequently driven by the size-related coordination preferences of the *A* site cations. The comparison between the Bi- and *Ln*-based ferrites shows that the introduction of the large cation Ba^{2+} produces a cation ordering in the two families, e.g. $YBaFe_2O_5$ [37] or $YBa_2Fe_3O_8$ [38] and $(Ba_{2-3x}Bi_{3x-1})(Fe_{2x}Bi_{1-2x})O_{2+3/2x}$ [21–23], whereas no similar effect has been reported for $Ae = Sr$, Ca in the homologous $Ln_{1/3}Ae_{2/3}FeO_{2.67}$ [29–40] and $Ln_{1/2}Ae_{1/2}FeO_{2.75}$. Although La^{3+} and Bi^{3+} have close ionic radii, the Fe^{3+}-based ferrites exhibit different superstructures and the present study highlights the role of Bi^{3+} on the structure modifications. The magneto-transport measurements show that the trivalent state of iron remains the main parameter, which governs the magnetic properties, whatever the cation arrangement.

A simple model has been proposed based on these different pieces of information, which is consistent with those obtained on the commensurate $Bi_{1/2}Ba_{1/2}FeO_{2.75}$, which exhibits disordered and non-disordered zones [23]. In the present compounds, the Mössbauer analyses show that the situation is highly more complex than in the Ba-based ferrite [22]. This is reinforced by the fact that the *ab initio* attempts for refining an accurate structure from X-ray powder data failed. The order/disorder phenomena and the complex environments of iron, which take place in these $Bi_{1/3}Sr_{2/3}FeO_{2.67}$ and $Bi_{1/2}Ca_{1/2}FeO_{2.75}$ perovskites, need to combine XRPD and NPD data to be solved. This work will be carried out in two steps, the first one being a neutron diffraction study at high temperature in order to refine the structure in the paramagnetic state.

$Bi_{1/3}Sr_{2/3}FeO_{2.67}$ and $Bi_{1/2}Ca_{1/2}FeO_{2.75}$ behave different compared to their *Ln*-based homologous, as $BiFeO_3$ with regard to the $LnFeO_3$ ferrites. One of the clues is the role played by the bismuth; it is therefore important to understand the structural mechanisms that govern the ordering phenomena of these ferrites.

Acknowledgments

The authors acknowledge financial support from the European Union under the Framework 6 program under a contract for an Integrated Infrastructure Initiative. Reference 026019 ESTEEM and thank Dr. J. Hadermann for her collaboration.

The authors thank Dr. D. Grebille for his help in the single-crystal X-ray diffraction studies.

References

[1] S. Galasso, Structure, Properties and Preparation of Perovskite Type Compound, Pergamon Press, Oxford, 1969.
[2] Roger. H. Mitchell, Perovskites, Modern and Ancient, Almaz Press, Thunder Bay, 2002.
[3] E.F. Bertaut, P. Blum, A. Sagnieres, Acta Crystallogr. 12 (1959) 149.
[4] Y. Takeda, K. Kanno, T. Takada, O. Yamamoto, M. Takano, N. Nakayama, Y. Bando, J. Solid State Chem. 63 (1986) 237.
[5] J.C. Grenier, M. Pouchard, P. Hagenmuller, Struct. Bonding 47 (1981).
[6] J.C. Grenier, N. Ea, M. Pouchard, P. Hagenmuller, J. Solid State Chem. 58 (1985) 243.
[7] M. Takano, T. Okita, N. Nakayama, Y. Bando, Y. Takeda, O. Yamamoto, J.B. Goodenough, J. Solid State Chem. 73 (1988) 140.
[8] J.P. Hodges, S. Short, J.D. Jorgensen, X. Xiong, B. Dabrowski, S. Mini, C.W. Kimball, J. Solid State Chem. 151 (2000) 190.
[9] C. Greaves, A.J. Jacobson, B.C. Tofield, B.E.F. Fender, Acta Crystallogr. B 31 (1975) 641.
[10] P.M. Woodward, D.E. Cox, E. Moshopoulo, A.W. Sleight, S. Morimoto, Phys. Rev. B 62 (2000) 844.
[11] Y.M. Zhao, M. Hervieu, N. Nguyen, B. Raveau, J. Solid State Chem. 153 (2000) 140.
[12] I. Sosnowska, R. Przenioslo, P. Fisher, V.A. Murashov, J. Magn. Magn. Mater. 160 (1996) 384.
[13] P.K. Gallagher, J.B. Mac Chesney, D.N.E. Buchanan, J. Chem. Phys 41 (1964) 2429.
[14] T. Takeda, S. Komura, H. Fujii, J. Magn. Magn. Mater. 31–34 (1983) 797.
[15] Y.M. Zhao, P.F. Zhou, J. Magn. Magn. Mater. 281 (2004) 214.
[16] Y.M. Zhao, R. Mahendiran, N. Nguyen, B. Raveau, R.H. Yao, Phys. Rev. B 64 (2001) 024414.
[17] P. Adler, A. Lebon, V. Damljanovic, C. Ulrich, C. Bernhard, A.V. Boris, A. Maljuk, C.T. Lin, B. Keimer, Phys. Rev. B 73 (2006) 094451.
[18] E.K. Hemery, G.V.M. Williams, H.J. Trodahl, Phys. Rev. B 75 (2007) 092403.
[19] C. Michel, J.M. Moreau, G.D. Achenbach, R. Gerson, W.J. James, Solid State Commun. 7 (1969) 701.
[20] A.J. Jacobson, B.E.F. Fender, J. Phys. C, Solid State Phys. 8 (1975) 844.
[21] M. Zanne, C. Gleitzer, J. Aubry, J. Solid State Chem. 14 (1975) 160.
[22] Ph. Boullay, M. Hervieu, N. Nguyen, B. Raveau, J. Solid State Chem. 147 (1999) 45.
[23] Ph. Boullay, D. Grebille, M. Hervieu, B. Raveau, E. Suard, J. Solid State Chem. 147 (1999) 450.
[24] C. Chaillout, A. Santoro, J.P. Remeika, A.S. Cooper, S.P. Espinosa, S.P. Marezio, Solid State Commun. 65 (1988) 1363.
[25] C. Bougerol-Chaillout, P. Bordet, S. Kazakov, J. Pshirkov, S.N. Putilin, E.V. Antipov, M. Nunez-Regueiro, Physica C 341–348 (2000) 1813.
[26] J. Li, Y. Duan, H. He, D. Song, J. Alloys Compd. 315 (2001) 259.
[27] V.A. Khomchenko, D.A. Kiselev, J.M. Vieira, A.L. Kholkin, M.A. Sa, Y.G. Pogolrelov, Appl. Phys. Lett. 90 (2007) 242901.
[28] V. Petricek, M. Dusek, L. Palatinus, JANA2006. The Crystallographic Computing System. Institute of Physics, Praha, Czecg Republic, 2007.
[29] P.D. Battle, T.C. Gibb, P. Lightfoot, J. Solid State Chem. 84 (1990) 237.
[30] F. Varret, J. Teillet, “MOSFIT” unpublished programme, Université du Maine, France.
[31] A. Altomare, M.C. Burla, M. Camalli, B. Carrozzini, G.L. Cascarano, A. Guagliardi, C. Giacovazzo, A.G.G. Moliterni, G. Polidori, R. Rizzi, EXPO: a program for full powder pattern decomposition and crystal structure solution, J. Appl. Crystallogr. 32 (1999) 339.
[32] P.D. Nellist, S.J. Pennycook, Ultramicroscopy 78 (1999) 111.
[33] W.C. Koehler, E.O. Wollan, J. Phys. Chem. Solids 2 (1957) 100.
[34] W.C. Koehler, E.O. Wollan, M.K. Wilkinson, Phys. Rev. 118 (1) (1960) 58.
[35] P.D. Battle, T.C. Gibb, P. Lightfoot, J. Solid State Chem. 84 (1990) 271.
[36] H.W. Brinks, H. Fellvag, A. Kjekshus, B.C. Hauback, J. Solid State Chem. 150 (2000) 233.
[37] L. Righi, M. Amboage, J. Gutierrez, J.M. Barandiaran, L. Fernandez Barquin, M.T. Fernandez Diaz, Physica B 276 (2000) 718.
[38] P. Karen, P.M. Woodward, J. Mater. Chem. 9 (1999) 789.
[39] P. Karen, A. Kjekshus, Q. Huang, J.W. Lynn, N. Rosov, I.N. Sora, V.L. Karen, A.D. Mighell, A. Santoro, J. Solid State Chem. 136 (1998) 21.
[40] M. Alario Franco, M.J.R. Henche, M. Vallet, J.M.G. Calbet, J.C. Grenier, A. Wattiaux, P. Hagenmuller, J. Solid State Chem. 46 (1983) 23.